

Long-time evolution of interfacial structure of partial wetting

Mengfei He ^{*}

Department of Physics, The James Franck and Enrico Fermi Institutes, The University of Chicago,
Chicago, Illinois 60637, USA



(Received 31 October 2019; accepted 11 August 2020; published 9 November 2020)

When a solid plate is withdrawn from a partially wetting liquid, a liquid layer dewets the moving substrate. High-speed imaging reveals alternating thin and thick regions in the entrained layer in the transverse direction at steady state. This paper systematically compares this situation to the reversed process, forced wetting, where a solid entrains an air layer along its surface as it is pushed into a liquid. To quantify the absolute thickness of these steady-state structures precisely, I have developed an optical technique, taking advantage of the angle dependence of interference, combined with a method based on a maximum-likelihood estimation. The data show that the thicknesses of both regions of the film scale with the capillary number, Ca . Further, an additional region is observed during onset, the quantitative explanation of which requires future investigation.

DOI: [10.1103/PhysRevFluids.5.114001](https://doi.org/10.1103/PhysRevFluids.5.114001)

I. INTRODUCTION

In “forced wetting,” a solid substrate rapidly enters a liquid bath with a film of air entrained along its surface [Fig. 1(a)]. The liquid *wets* the solid. Conversely, in “dewetting,” a solid is rapidly withdrawn from a liquid bath, dragging out a film of liquid [Fig. 1(b)]. The liquid film *dewets* the surface as it is pulled down by gravity. This paper shows that forced wetting and dewetting share many similarities.

The phenomenon of forced wetting or dewetting can be observed commonly in daily life. Yet, it can often be difficult to see the steady-state behavior of forced wetting or dewetting, as distinct from capturing only the initial onset. In order to characterize the long-time limit of forced wetting, we developed a system in our previous study [1] to maintain the entrained air layer until a steady state is reached. By steadily pushing a long ribbon of mylar tape into a liquid, the air layer develops prominent and surprising structures. Figure 1 (inset A) shows that at steady state, the air layer assumes a V shape with two extremely flat and thin sections positioned at the upper corners.

This paper extends this study to the process of dewetting. Figure 1 (inset B) shows that at steady state, the entrained liquid layer forms an upside-down V shape. Both in the case of dewetting and wetting (as shown in Ref. [1]), two sharply different thicknesses stably coexist inside a triangular-shaped contact line (the solid/liquid/gas interface). There is a thin-thick alternation of the entrained fluid that appears near the bottom (in dewetting) or near the top (in wetting) across the width of the substrate. Despite the well-known fundamental difference in advancing and receding contact-line motions [2], there is a striking similarity between the structures found in both experiments.

The study of wetting and dewetting began long before the age of high-speed imaging [3,4]. Various aspects have been addressed such as deposited layer thickness [5–8], maximum wetting speed [9–15], contact angles [16–19], confinement effects [20–22], and the *onset* of the entrainment transition [23–29]. The main purpose of this paper, on the other hand, is to study the long-time

*mhe100@syr.edu

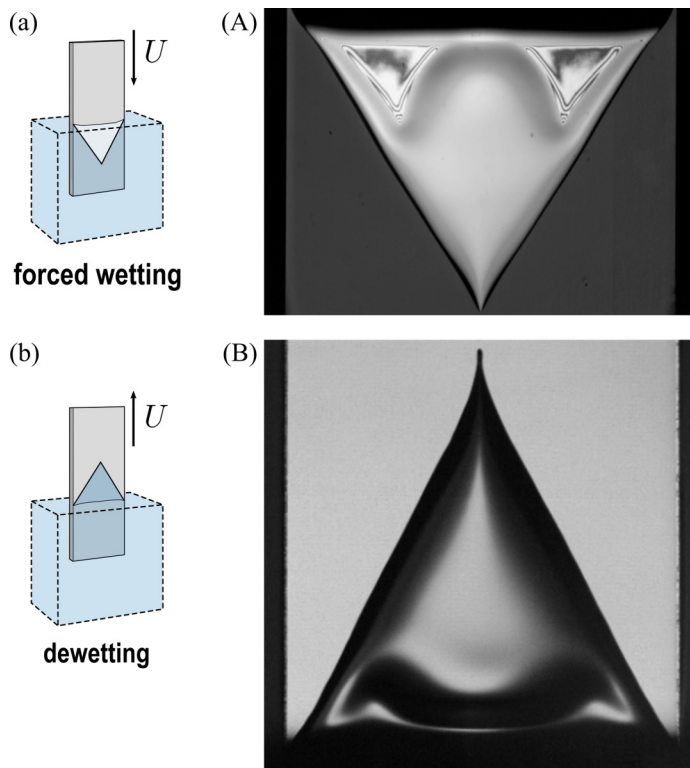


FIG. 1. (a) Schematic of forced wetting. A film of air is entrained into a liquid bath by the surface of a moving substrate. Inset A: Front view of the steady state of an entrained air film in forced wetting. A mylar tape of width $w = 12.7$ mm plunges vertically into a water-glycerin mixture of viscosity $\eta_{\text{out}} = 226$ cP at $U = 130$ mm/s. The entrained air layer assumes a V shape with two thin, flat sections at the upper corners. (b) Schematic of dewetting. A film of liquid is dragged out from a liquid bath by the surface of a moving substrate. Inset B: Front view of the steady state of a liquid film in dewetting. An acrylic plate of width $w = 20.3$ mm is pulled vertically out of a water-glycerin bath of viscosity $\eta = 100$ cP at $U = 4.4$ mm/s. An entrained liquid layer forms an upside-down V shape with two thin sections at the lower corners.

evolution of the contact-line motion, and to characterize the prominent structure in the entrained fluid layer at steady state. By measuring interference fringes as a function of the angle of incidence of the light source, the *absolute* thickness of the wetting layer was determined as a function of different control parameters.

Forced wetting or dewetting can occur in different geometries [30–34]. Notably, a series of studies shows that the tail of a sliding droplet is in many aspects an equivalent problem [35–43]. The observations and conclusions presented in the present work may suggest similar behavior in those situations and contribute an alternative perspective for wetting and dewetting in its various other forms.

II. EXPERIMENTS

A. Mechanical apparatus, fluids, and substrate preparation

For the dewetting experiments, the solid substrate was installed on a stage on a vertical linear guide (PBC Linear™, Integral-V Technology; Rail system: AAW). The system was driven by a step motor (Silverpak 17) through a roller chain. The substrate velocity ranged from 1 to 400 mm/s

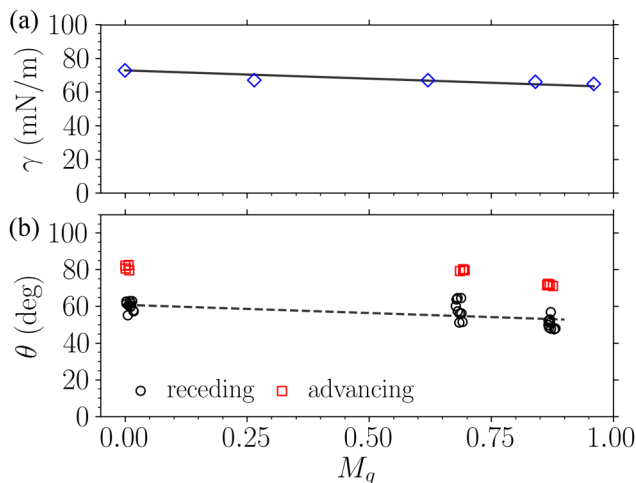


FIG. 2. (a) Measured liquid-air interfacial tension γ versus glycerin mass fraction M_g of water-glycerin mixtures. Solid line, prediction of Eq. (1). (b) Receding and advancing contact angles on an acrylic substrate (Rain-X[®] coated) versus M_g . At each value of M_g , the data are displaced slightly in the x direction to make overlapping symbols visible. Dashed line, linear fit for receding contact angles.

with <5% fluctuation. Water-glycerin mixtures were used as the viscous liquid with a viscosity range $0.9 \leq \eta \leq 1264$ cP. The viscosity was measured by an Anton Paar MCR301 rheometer or by manual glass viscometers (CANNON-Ubbelohde). The density ρ and the liquid-air interfacial tension γ of the mixture were measured by a KRÜSS tensiometer, which were consistent with literature values [44,45]. The measured γ 's are plotted in Fig. 2(a), where the solid line shows that they can be well described by the fractional contribution model [45],

$$\gamma = M_g \gamma_g + (1 - M_g) \gamma_w, \quad (1)$$

where M_g is the mass fraction of the glycerin in the mixture, γ_g the surface tension of pure glycerin, and γ_w the surface tension of pure water. The relation between η and the mass fraction M_g of the glycerin in the mixture is well known [46] and is consistent with the measurements.

In the dewetting experiments, the solid substrate consists of slender rectangular sections (560 mm \times 3.2 mm) of black cast acrylic, cut to various widths, $12.3 \leq w \leq 50.5$ mm. The edges were further milled and polished to prevent contact-line pinning during the experiments. The substrate surface was first wiped with isopropyl alcohol to remove chemical residues from the manufacturing process. Rain-X[®] Original Glass Water Repellent (PDMS) was then applied to the surface and then wiped off. I found the wetting and dewetting configuration to be more reproducible when the prepared surface has fully interacted with the water-glycerin mixture. Therefore, a few wetting/dewetting cycles were carried out before any data were taken, to saturate any transient or “aging” effect. The static contact angles were measured from side-view images of the drops of the mixtures against the prepared acrylic substrate, shown in Fig. 2(b) [47]. The advancing values (red squares) were measured from the drops soon after they were deposited onto the substrate. To obtain the receding values (black circles), the contact line of a drop was made to move at a negligible velocity ($<50 \mu\text{m/s}$) by continuously adding or removing liquid through a needle, and the data scatter in Fig. 2(b) reflects the fluctuations of the stick-slip motion. Following le Grand *et al.* [37], circles were fitted locally whose tangent lines were found $\sim 30 \mu\text{m}$ near the contact lines to ensure reproducibility of the angle measurements. As can be seen in Fig. 2(b), the gaps between the advancing and receding contact angles show a significant contact angle hysteresis of $\sim 20^\circ$ of water-glycerin mixtures on the Rain-X[®] coated acrylic. A linear fit (dashed line) gives an empirical

formula:

$$\theta_r = 60.78^\circ - 8.9^\circ M_g. \quad (2)$$

Both γ and θ_r are nearly constants in the experimental range, the weak decreasing trend of which can be sufficiently characterized by the linear approximations in Eqs. (1) and (2). As will be shown in Sec. III B, γ and θ_r have limited impact on the data analysis.

For the forced-wetting experiments, commercial magnetic mylar tape (cassette tape with $w = 6.4$ mm, VHS tape with $w = 12.7$ mm, and recording tape with $w = 25.4$ mm) was used as the substrate. A water-glycerin mixture was used as the outer fluid with viscosity $26 \leq \eta_{\text{out}} \leq 572$ cP.

Measurement of the refractive index (consistent with the literature [48]) and the thickness of the entrained liquid layer are described below and in Ref. [49].

B. Measurement of absolute film thickness

Haidinger's fringes, to be distinguished from Newton's fringes, refer to the interference pattern produced by a varying angle of incidence, θ , of the light source [50,51]. To obtain the *absolute* thickness, h , of an entrained fluid layer, I have developed an interferometric method based on measuring Haidinger's fringes given by the sample. h affects how the optical path difference, ΔL , changes with θ . By measuring ΔL (or equivalently, the interference intensity) as a function of θ at a given point, h at that point can be deduced. The measuring device is similar to one used to measure the thickness of oxide layers and silicon semiconductor samples [52,53]. The derivation of the principle is shown in Appendix A and the features and capabilities of this method are described in Ref. [49].

To map the detected interference pattern to sample thickness h , I have developed an algorithm using likelihood maximization (Appendix B). This algorithm facilitates a reliable pattern detection and a precise topography reconstruction.

Combining the above techniques, I am able to identify precisely the absolute thickness of the entrained fluid layer systematically.

III. RESULTS

A. Formation of a V-shaped structure

Figure 3 shows a series of images of a fluid being pulled out of a bath by a flat substrate with straight edges. The substrate travels vertically upward at a constant velocity while the liquid forms a thin layer entrained to its surface. Initially, as shown in the first frame [Fig. 3(a)], the contact line rises from the bath in the form of a trapezoid composed of a central nearly horizontal section with two short sloping sides. In the second frame [Fig. 3(b)], the trapezoid grows in height. The sides remain at the same angle and the central horizontal section advances upward and becomes narrower. Just behind the contact line there is a thick ridge; further back there is an extended thin, flat region. In the third frame [Fig. 3(c)] the horizontal contact line moves upward until the trapezoid closes into a triangle. At this point, the central part of the thick ridge starts to widen and spread downward. In the final frame [Fig. 3(d)], as the system reaches its steady-state shape, the thin part is split into two smaller sections at the lower corners of the entrained fluid.

There appears a thin-thick alternation in the spanwise direction near the bottom of the entrained layer. In steady state, as shown in the fourth image [Fig. 3(d)], the triangular contact line retracts slightly so that the tilted sides are less steep compared to its shape during formation shown in the third frame. When the velocity of the substrate is large enough, small liquid drops, attached to the moving substrate, emerge at the tip of the triangular pocket, also shown in the last frame [Fig. 3(d)].

The number of alternating undulations of the layer thickness in the transverse direction depends on the width of the substrate. Figure 4(a) shows steady state of a forced wetting film on a mylar surface of width $w = 25.4$ mm. Compared to Fig. 1(a) (substrate width $w = 12.7$ mm), Fig. 4(a)

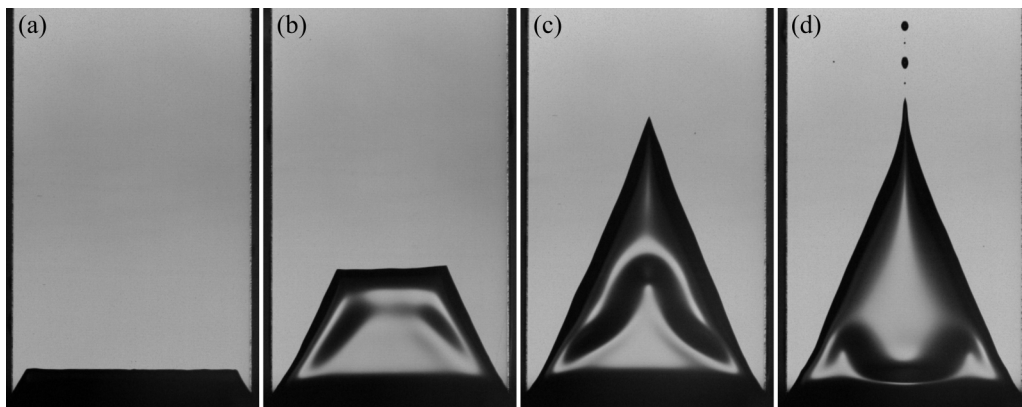


FIG. 3. Images of a typical evolution of a dewetting liquid layer, for a duration of ≈ 40 s. An acrylic plate of width $w = 20.3$ mm is pulled vertically out of a water-glycerin bath of viscosity $\eta = 100$ cP at $U = 4.4$ mm/s. The fluid layer reaches its steady state in (d). (The images in (a)–(d) are not evenly spaced in time in order to show the different stages clearly.)

shows that near the top of the V there are four thin sections. The thin-thick features are more extended for wider substrates than they are for narrower ones.

The same trend applies for the case of dewetting. Figure 4(b) shows that the dewetting film contains multiple marked thin-thick alternations for a $w = 35.3$ mm wide acrylic plate.

To quantify this trend, I measured in dewetting the width of the thick bulge W as indicated by the dashed line in Fig. 4(b). Figure 5(a) shows that this width does not remain a constant with increasing substrate width. For wide substrates, $w > 70$ mm in the case of water dewetting on mylar, the adjacent thick parts constantly merge and resplit, so the width of a single bulge fluctuates considerably. Despite these fluctuations, Fig. 5(b) shows that there is a linear relationship between the number of thick bulges versus the substrate width w .

The front-view shape of the thick bulges in forced wetting, on the other hand, is very well defined. A large portion near the tip of the thick section can be approximated by a circle, as indicated in Fig. 4(a). In Fig. 6 I have plotted the measured radius, R , of the fitted circle, versus liquid viscosity η_{out} , for a fixed substrate width $w = 12.7$ mm. The error bars indicate the influence on R of different substrate velocities. The radius decreases with an increase of the liquid viscosity, and saturates at a value close to the capillary length $l_c = \sqrt{\gamma/\Delta\rho g}$, independent of the substrate velocity. This suggests that at a large viscosity ($\eta_{\text{out}} > 90$ cP) the shape of the thin-thick boundary of the air layer is selected by a balance between buoyancy and interfacial tension. The inset of Fig. 6 shows the superimposed images of two air layers entrained in two different viscous liquids (both with $\eta_{\text{out}} > 90$ cP). The two shapes have very different V-shaped outlines, but the curves of the thin-thick boundary overlap very well.

B. Wetting velocity of the contact line

The upside-down V shape of the contact line was first noted by Derjaguin and Levi [9], and was quantitatively interpreted by Blake and Ruschak in terms of the maximum velocity that a contact line could move across a substrate [12]. When the substrate velocity U exceeds the maximum value, U_{max} , the stationary contact must become inclined by an angle ϕ (with respect to the horizontal direction) so that the velocity of the contact line normal to its surface, U_n , remains at a constant value U_{max} :

$$U_n = U \cos \phi \leq U_{\text{max}}. \quad (3)$$

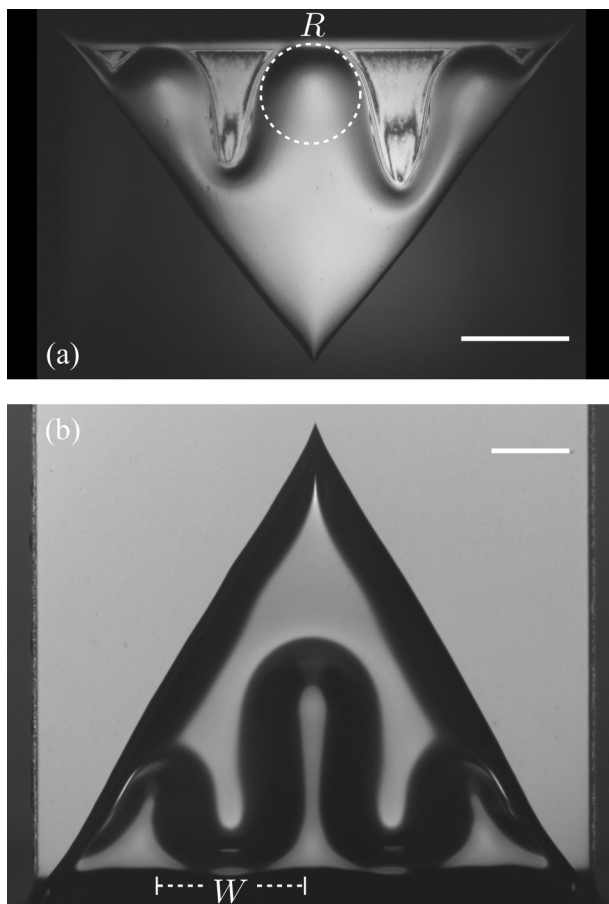


FIG. 4. Increasing substrate width w increases the number of thin-thick alternations in film thickness. (a) A 25.4-mm-wide recording tape entrains an air film with three thick sections. The upper portion of the thin-thick boundary can be approximated by a circle of radius R . (b) A 35.3-mm-wide acrylic plate entrains a water-glycerin film with two thick sections with width W . In (a) and (b) the substrate widths w are twice what they were in the corresponding images shown in Figs. 1(a) and 1(b). Scale bar: 5 mm.

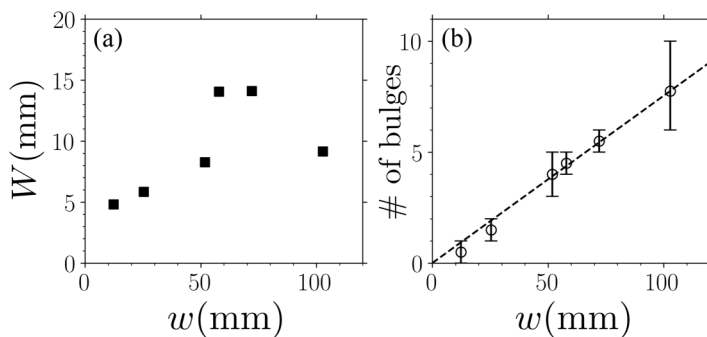


FIG. 5. Geometry of dewetting films. (a) Width of a thick section, W , versus substrate width, w , for water dewetting a mylar surface. (b) Number of thick parts, N , versus w , for water dewetting a mylar surface. Error bars indicate different thin-thick configurations observed, for a given w . Dashed line, linear fit to the mean observation.

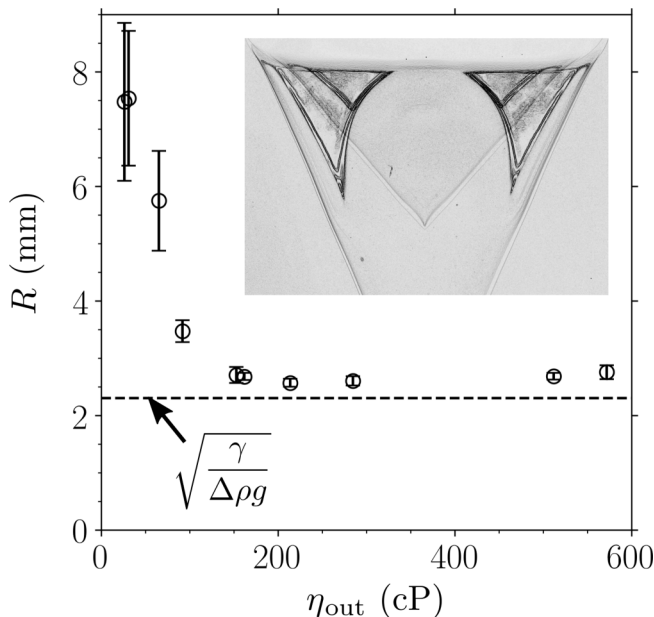


FIG. 6. Geometry of forced-wetting films. Radius of curvature, R , of the upper portion of the thick part is plotted against liquid viscosity η_{out} . Dashed line, capillary length $l_c = \sqrt{\gamma/\Delta\rho g}$. Inset: Superimposed edge-detected images of two different air films, entrained into different liquids of viscosities $\eta_{\text{out}} = 160$ and 290 cP, respectively, at $U = 150$ mm/s.

In this section, I show a few experimental observations on contact-line movement that imply more complexity than a simple model of a constant U_n .

For a typical experimental condition ($\eta = 100$ cP, $U = 4.4$ mm/s, $w = 20.3$ mm), Fig. 7(a) shows the inclination angle ϕ (relative to the horizontal direction) of the lateral contact line, tracked continuously over time t for seven repeated runs. Clearly ϕ and, therefore, U_n from Eq. (3) do not remain constant during the formation of the V shape. An obvious trend can be observed: the inclination first assumes an onset value ϕ_{on} , reaches a maximum, and plateaus at a steady-state value ϕ_{ss} . There are considerable fluctuations from run to run, but the variations do not show a time dependence (the order of runs is shown in the legend), ensuring no apparent “aging” effect of the Rain-X[®] coated substrate. A rough correspondence to the fluid shape imaged in Figs. 3(a)–3(d) is also noted in Fig. 7(a) (as I–IV). The maximum values of ϕ consistently occur at the completion of the triangular pocket shape [Fig. 3(c)]. Notice the extended duration of the experiments (~ 40 s) to reach steady state, which is much longer than that of forced wetting (~ 300 ms; see Fig. 1 of [1]), and often makes observation of steady state difficult in dewetting experiments. Since ϕ_{on} is consistently smaller than ϕ_{ss} , it is necessary to conduct separate analyses on both of these quantities. Motivated by Eq. (3), I plot in Figs. 7(b) and 7(c) $(\cos \phi)^{-1}$ versus U at onset and in steady state, respectively, for various liquid mixtures. The linear trends indicate that there exists a constant U_n independent of U for each viscosity, but the value is different at onset from what it is in steady state. The data for steady state in Fig. 7(c) depart significantly from linearity at larger velocities, possibly suggesting a different regime that I do not focus on in the present work. I fit the data to the relation $(\cos \phi)^{-1} = U_{n,\text{fit}}^{-1} U$ [Eq. (3)] for each liquid mixture. The resulting $U_{n,\text{fit}}$ is shown in Fig. 7(d), plotted versus η . The average normal velocity $U_{n,\text{fit}}$ is consistently larger at onset than it is in steady state as was noted above for the special case in Fig. 7(a). Observe that there is an approximate linear relationship in the log-log plot of Fig. 7(d), which motivates a power-law

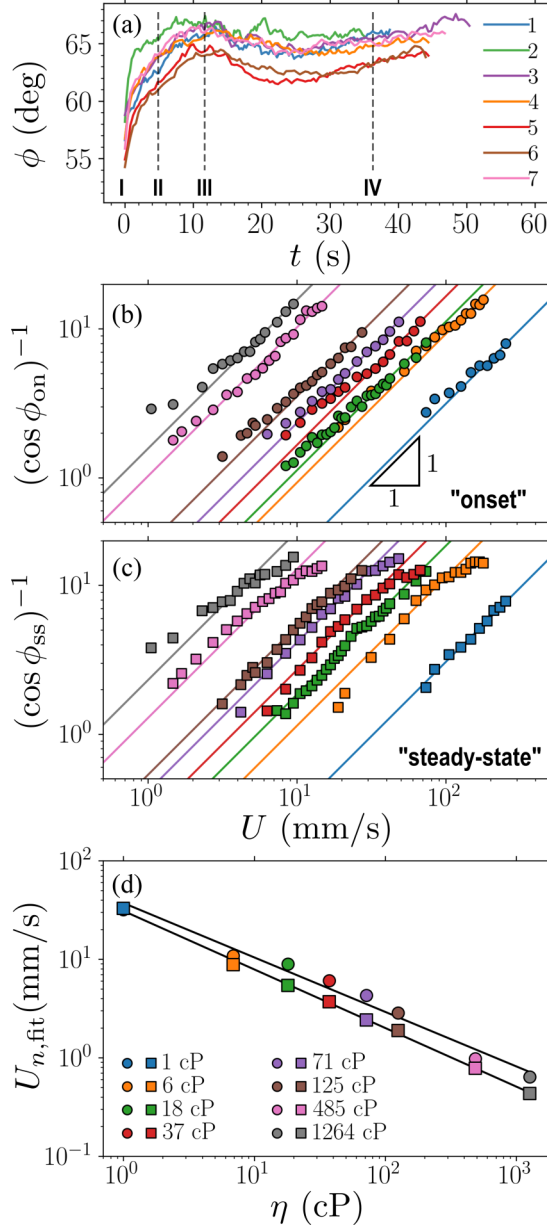


FIG. 7. Contact-line inclination and contact-line velocity in dewetting. (a) Evolution of the inclination angle ϕ (relative to the horizontal direction) of the lateral contact lines versus time t for seven different runs under the same condition. Plate velocity $U = 4.4$ mm/s. Liquid viscosity $\eta = 100$ cP. $(\cos \phi)^{-1}$ versus U for (b) onset (ϕ_{on} , circles) and (c) steady state (ϕ_{ss} , squares). Solid lines, linear fits to each data set (slope = 1). (d) Fitted normal relative velocity, $U_{n,\text{fit}}$, versus liquid viscosity η for both onset (circles) and steady state (squares). Top solid line, $U_{n,\text{fit}} \propto \eta^{-0.55}$; bottom solid line, $U_{n,\text{fit}} \propto \eta^{-0.59}$. Legend is consistent for (b), (c), and (d).

fit $U_{n,\text{fit}} \propto \eta^\alpha$:

$$U_{n,\text{fit,on}} \propto \eta^{-0.55 \pm 0.03}, \quad (4a)$$

$$U_{n,\text{fit,ss}} \propto \eta^{-0.59 \pm 0.01}. \quad (4b)$$

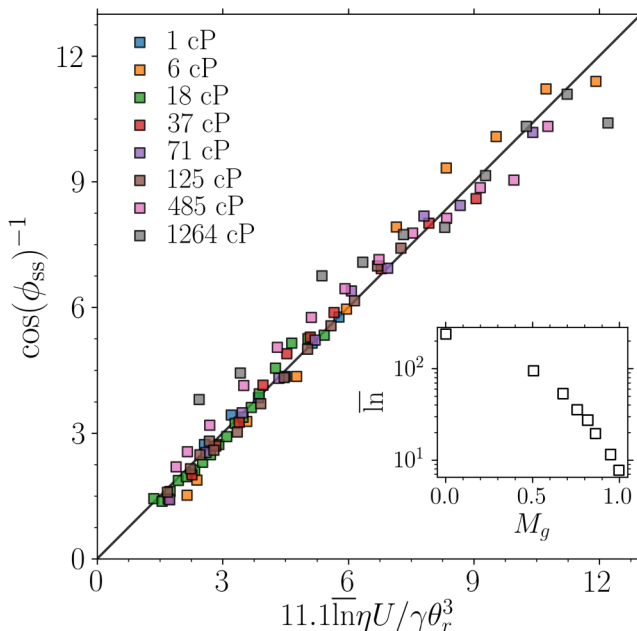


FIG. 8. Data collapsing for dewetting using Eq. (5). Only data from the linear regimes of Fig. 7(c) are used. Inset: Fitted $\overline{\ln}$ using Eq. (5) versus the glycerin mass fraction M_g .

Incorporating the surface tension γ or the static contact angle θ_r in the regression as $U_{n,\text{fit}} \propto \eta^\alpha \gamma^\beta$ or $U_{n,\text{fit}} \propto \eta^\alpha \theta_r^\beta$ shows that β is insignificantly different from zero [54]. The simple empirical laws in Eqs. (4a) and (4b) well describe the data for over three decades of viscosity η , as shown by the solid lines in Fig. 7(d). Yet it should be emphasized that Eqs. (4a) and (4b) are only phenomenological. The maximum wetting speed U_n may depend not only on η , γ , and θ_r but also the microscopic quantities such as the slip length l .

Usually [37], U_n is believed to be reached when the dynamic receding contact angle θ reaches some critical value θ_c . Combined with the classical Voinov-Cox description [55,56], the maximum wetting speed is $U_n = \gamma(\theta_r^3 - \theta_c^3)/9\eta\overline{\ln}$, where $\overline{\ln} \equiv \ln(x/l)$ is the logarithmic ratio of the macroscopic to microscopic scales. Observations on sliding droplets by le Grand *et al.* [37] suggest that this critical angle θ_c is close to the value $\theta_r/\sqrt{3}$, postulated long ago by de Gennes [57]. For simplicity, I assume $\theta_c = \theta_r/\sqrt{3}$, giving

$$U_n = \frac{\gamma}{\eta} \frac{\theta_r^3 - (\theta_r/\sqrt{3})^3}{9\overline{\ln}}. \quad (5)$$

Note Eq. (5) is not in immediate contradiction to Eqs. (4a) and (4b), because η , γ , θ_r , and $\overline{\ln}$ may all be related through the mixture fraction M_g . The simple model of Eq. (5) incorporates only local factors (θ_r , $\overline{\ln}$) and assumes steady state. Below, only data from steady state are tested. Since the slip length l cannot be directly measured from the current setup, $\overline{\ln}$ was used as a fitting parameter for Eq. (5), and the fitted result is shown in the inset of Fig. 8. It turns out that for the pure glycerin $M_g = 1$, the slip length $l = xe^{-\overline{\ln}} \sim 10^{-8}$ m is indeed in the nanometer scale corresponding to the molecular size. However, for all other water-glycerin mixtures, including pure water, $\overline{\ln}$ is unusually large and as a result $l \ll 10^{-9}$ m is unphysically small. Similar discrepancies have been found in experiments of sliding droplets of water [35,42].

After $\overline{\ln}$ is obtained, the data of Fig. 7(c) can be collapsed using Eqs. (3) and (5), as is shown in Fig. 8.

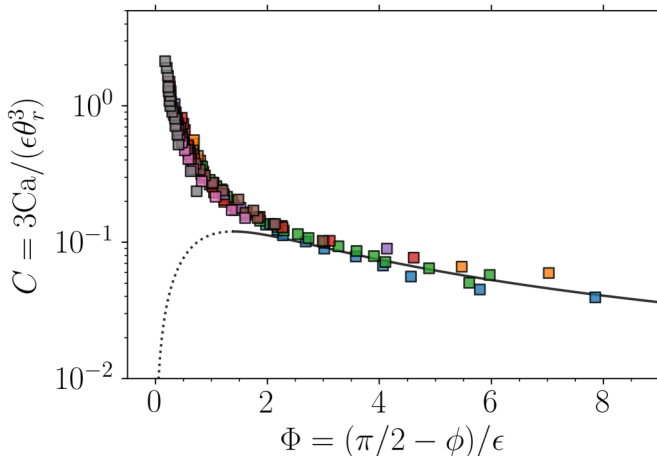


FIG. 9. Data collapsing for dewetting using Eq. (6). Legend consistent with Fig. 8. Dotted line, unstable branch of Eq. (6); solid line, stable branch.

Snoeijer *et al.* matched the contact-line dynamics with the similarity solution of a corner flow (Limat-Stone model [36,39]) for a sliding droplet, and found the relation [40]

$$C = \frac{6\Phi}{35 + 18\Phi^2}, \quad (6)$$

where $C = 3\eta U / (\gamma \epsilon \theta_r^3)$, $\Phi = (\pi/2 - \phi) / \epsilon$, and $\epsilon = 1 / \sqrt{\ln}$. Using the above fitting result of $\bar{\ln}$, despite the lack of its physical interpretation, the data in Fig. 7(c) can also be collapsed by Eq. (6), shown in Fig. 9. In the theory of Eq. (6), the stable branch only starts at $\Phi = \sqrt{35/18} \approx 1.4$ (solid line). In the unstable branch (dotted line) a rivulet solution takes place where the liquid is continuously deposited through a thin stream (which would further break into sessile droplets) at the tip of the V, as observed in Fig. 3(d). It is difficult to quantitatively verify the onset of the rivulet solution at $\Phi \approx 1.4$ here using the current imaging resolution and frame size for the V shape. A rough estimate suggests that the “pearling transition” takes place at $\Phi > 1.4$. Interestingly, the data collapse works for the whole range of Φ , for both the supposed corner regime (solid line) and the rivulet regime (dotted line). I find that the data collapse as well as the size of $\bar{\ln}$ do not depend too critically on the model of Eq. (5), although it indeed gave a somewhat better collapse compared with several other hydrodynamic variations (Voinov and Cox [55,56], Dussan [58], de Gennes and Brochard-Wyart [57,59], and Eggers [23]). In the meantime, I point out that Eq. (6) is not trivially equivalent to Eq. (5) (only equivalent if $\Phi \gg 1.4$ [39]) for my experimental regime so that the collapse is not automatic. Curiously, Eq. (6) was based on a self-similar flow without gravity effect for a sliding droplet, yet works for plate dewetting here of a more complex geometry (thin-thick alternation) and a larger length scale, suggesting that the underlining dynamics may be closely related.

For the case of steady-state forced wetting, our previous work [1] concluded a power law for the relation between the normal wetting velocity, U_n , versus the viscosity of the *outer* liquid, η_{out} , where an air pocket is entrained into:

$$U_n \propto \eta_{\text{out}}^{-0.75 \pm 0.03}. \quad (7)$$

Therefore, the normal relative velocity, U_n , decreases with increasing viscosity both in the case of the inner fluid (as in the case of dewetting) and for the outer fluid (as in wetting).

Kamal *et al.* [29] studied the contact-line motion where the inner and outer fluids have comparable contributions to the dynamics. This is the case for forced wetting near the contact line. Although

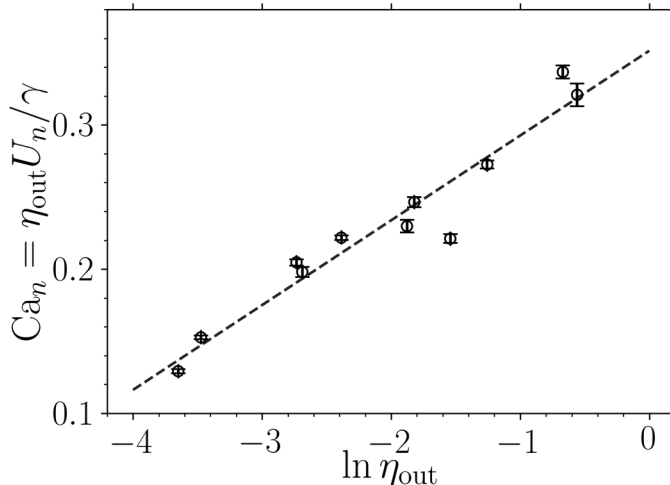


FIG. 10. Forced wetting data plotted as Ca_n versus $\ln \eta_{out}$. Solid line: a least-squares fit shows a good linear relation.

air has a much smaller viscosity than the viscous liquid, its dissipation cannot be neglected because of the sharp wedge near the contact line (see also Refs. [28,60,61]). In their theoretical work they concluded a logarithmic behavior:

$$Ca_n \equiv \frac{\eta_{out} U_n}{\gamma} = C_1 \ln \eta_{out} + C_2, \quad (8)$$

where C_1, C_2 are constants depending on the model details. To compare with Eq. (8), I plotted Ca_n versus $\ln \eta_{out}$ in Fig. 10 using the same data leading to the empirical relation Eq. (7). The linear relationship in Fig. 10 indicates Eqs. (7) and (8) are compatible, and our data in forced wetting verifies the logarithmic trend [62].

Finally I show a visualization of the transition of the velocity of the nearly horizontal contact line, by continuously tracking the contact-line position through a high-speed camera. For a typical dewetting process, Fig. 11(a) shows the superimposed positions of the contact line at equal time intervals until the trapezoid has reached the triangular shape as seen in Fig. 3(c). The normal relative velocity $U_n(x, y)$ can then be calculated at each point (x, y) at the contact line [illustrated in the inset of Fig. 11(a)]:

$$U_n(x, y) = [U - U_{cl}(x, y)] \cos \varphi(x, y), \quad (9)$$

where U is the plate velocity, U_{cl} is the vertical velocity of a contact-line element at (x, y) , and $\varphi(x, y)$ is the *local* inclination of the contact line. In Fig. 11(a), the calculated magnitude field $U_n(x, y)$ swept out by the nearly horizontal contact line during this period is mapped in the same figure to a color scale. The color map shows a significant decrease in normal relative velocity, U_n , throughout the process, which is consistent with the above fitted result $U_{n,fit,on} > U_{n,fit,ss}$ for the lateral contact lines. The same conclusion applies for the case of forced wetting, as shown in Fig. 11(b). Note a velocity change of the horizontal contact line soon after entrainment has been observed and modeled with a quasisteady lubrication theory [24,25]. The current work further extends the observation till steady state.

Previous studies show that there is no universal contact-line velocity among wetting and dewetting processes in different geometries. For example, in plate withdrawal at different angles, droplet sliding, or rupture hole expansion, different dewetting velocities have been reported [24,25,40,61]. This is because typically the wetting or dewetting velocity is determined not only by the local flow

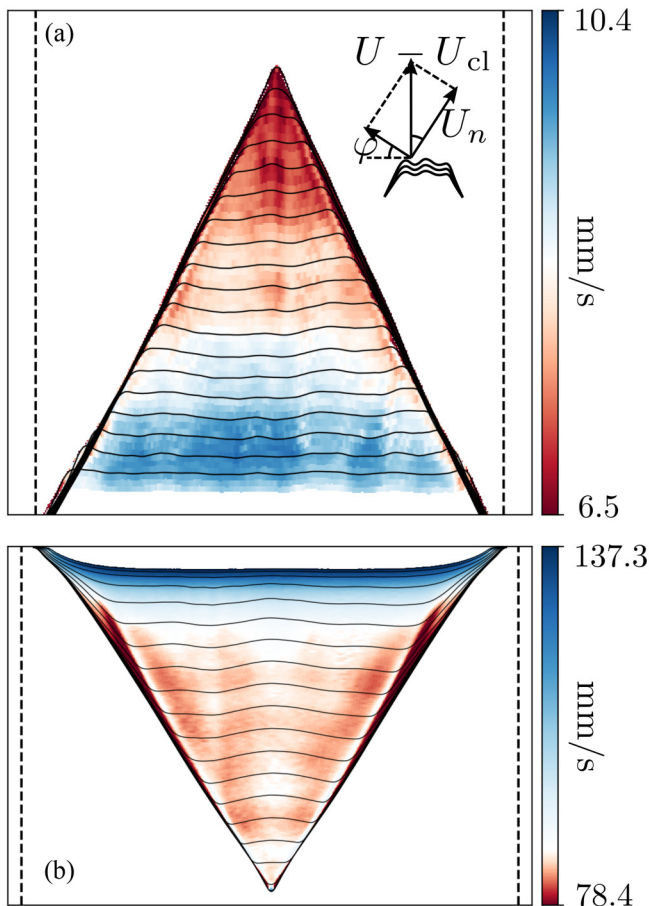


FIG. 11. Normal relative velocity, U_n , of contact line during formation of a V. Color scale: U_n deduced from Eq. (9). (a) Contact-line positions at intervals of 100 ms, for an acrylic moving out of a water-glycerin mixture of viscosity $\eta = 18$ cP at $U = 15.8$ mm/s. (b) Contact-line positions at intervals of 50 ms, for a mylar moving into a water-glycerin mixture of $\eta_{\text{out}} = 226$ cP at $U = 130$ mm/s.

in the vicinity of the contact line, but also by a matching to the outer large-scale geometry [23,63]. The change of the contact-line velocity from the onset to steady state, observed in the current work, could potentially be ascribed to a change of the outer geometry (shape of the entrained film), which cannot be captured by simplified local models such as in Eq. (5).

C. Thickness structure of wetting layer

Figure 12 shows the measurements of the thin and thick regions of the dewetting layer. The first row shows a measurement at one point of the thin, flat part. In the image shown in the top left panel, the arrow and white spot indicate the position where the measurement is taken: near the bottom middle of the frame. The top middle panel shows the circular fringes from the high-speed camera. Using the method of maximum-likelihood estimation allows clear identification of the interference rings; the top right panel shows the reconstructed pattern $X_0(x, y, \beta_{\text{optimal}})$ (see Appendixes A and B and Ref. [49]). The thickness of the entrained layer in this region is $h_{\text{optimal}} = 84.2 \mu\text{m}$. Similarly the second row shows a measurement of the thick part of the entrained fluid when it expands to touch the bottom with the measurement placed near the bottom right as shown by the arrow. A

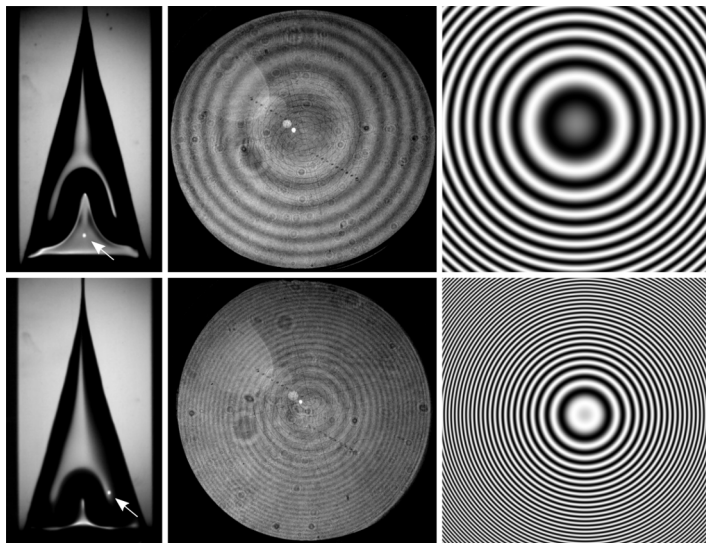


FIG. 12. Thickness fitting by likelihood maximization. An acrylic substrate travels out of a liquid of viscosity $\eta = 18$ cP at $U = 17$ mm/s. Left column is an image of the entrained fluid. The arrows pointing to focusing spots indicate location of the measurement. Middle column: Corresponding interference fringes (Haidinger's fringes; see Appendix A and Ref. [49]) captured by high-speed camera. Right column: Reconstructions of fringes using maximizing likelihood (see Appendix B), giving thicknesses of $h = 84.2$ μm for the thin region (top row) and 285.0 μm for the thick region (bottom row).

thicker fluid layer gives rise to a much denser set of fringes, and the maximum-likelihood fitting gives $h_{\text{optimal}} = 285.0$ μm .

To see the dependence of the steady-state thickness h on the substrate width w , I measured the thickness of both the thin and thick regions for various substrate widths. As shown in Fig. 13(a), when w is varied, h of the thick region fluctuates, but does not show an apparent general trend. The thin part becomes slightly thicker ($\sim 20\%$) as the width w is increased by a factor of ~ 5 . Therefore, the thickness h for both the thin and thick parts is nearly independent of the plate width w . In the following, I focus on one plate width w only in measuring the thicknesses.

Figure 13(b) shows a typical configuration of the liquid layer entrained on a wide substrate, while Fig. 13(c) shows a zoomed-in image of the thin-thick alternation region, obtained using a sodium-vapor lamp (wavelength $\lambda = 589$ nm). Because of a long coherence length of the light source, interference patterns appear in the thin parts. An order of ~ 10 fringes can be detected in each thin part so one can estimate the thickness variation to be ~ 3 μm , much smaller than the thickness itself. It shows that the thin parts are very flat, and measuring thickness at one point only is sufficient in characterizing the thin-part thickness.

For a fixed substrate width, w , Fig. 14 shows the measurements in the dewetting steady state of the thin and thick regions as a function of liquid viscosity η and substrate velocity U . As is shown for both regions, h , normalized by the capillary length $l_c = \sqrt{\gamma/\Delta\rho g}$, is approximately a power law in the capillary number, $\text{Ca} = \eta U/\gamma$:

$$h/l_c \propto \text{Ca}^\alpha. \quad (10)$$

For over two orders of magnitude in Ca , I find for the thick part

$$\alpha_{\text{thick}} = 0.46 \pm 0.01. \quad (11)$$

This result can be understood by a similar argument as was used for the reversed situation of wetting [1]. The complex-shaped liquid layer can be simplified as a wedge with an average wedge

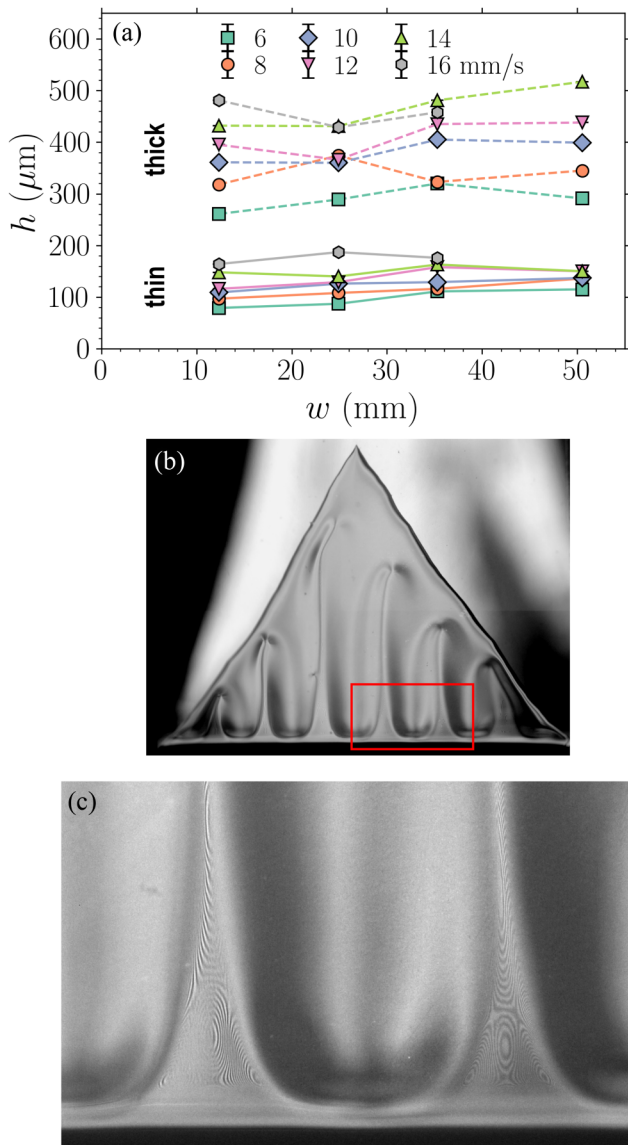


FIG. 13. (a) Thickness h for steady state of dewetting, versus substrate width w . Markers connected by solid lines, thin part; markers connected by dashed lines, thick part. Liquid viscosity $\eta = 41$ cP. (b) A typical configuration of the entrained liquid layer on a wide substrate. (c) Zoomed-in view of the indicated region (red square) in (b). Sample illuminated by a sodium-vapor lamp (wavelength $\lambda = 589$ nm). Interference stripes in the thin regions indicate the flatness.

angle, Θ , where it meets the substrate. Using the result of Huh and Scriven [60] that the interface velocity U_I is proportional to the substrate velocity U ,

$$U_I = \zeta \left(\frac{\eta_{\text{in}}}{\eta_{\text{out}}}, \Theta \right) U, \quad (12)$$

where η_{in} is the viscosity of the inner fluid (water-glycerin mixture) and η_{out} is the viscosity of the outer fluid (air). In the limit of large $\eta_{\text{in}}/\eta_{\text{out}}$ (10^2 – 10^5) and small Θ (<90), it can be shown

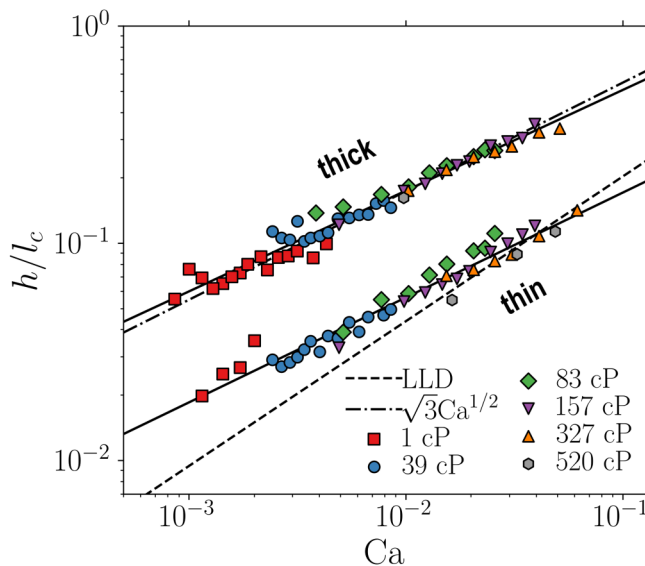


FIG. 14. Thickness for dewetting layers normalized by capillary length, h/l_c , versus capillary number Ca , for both the thin parts and the thick parts. Top solid line, $h/l_c \propto Ca^{0.46}$; bottom solid line, $h/l_c \propto Ca^{0.48}$; substrate width, $w = 17.1$ mm.

that the proportionality ζ is approximately a constant, nearly independent of η_{in}/η_{out} and Θ . Using the average value of the measured static receding contact angle 63° as an approximation to the dynamic contact angle Θ , we get $\zeta = -0.557 \pm 0.005$. The negative sign indicates that the flow at the interface is in the opposite direction of the substrate motion, about half in magnitude. I argue that the thickness is selected by maximum stability of the layer, so that Eq. (7) of Ref. [1] can be directly applied:

$$\begin{aligned} h_{\text{thick}} &= \left(2(1 - \zeta) \frac{\eta_{in}}{\Delta\rho g} U \right)^{\frac{1}{2}} \\ &= \sqrt{3} \cdot 1l_c Ca^{\frac{1}{2}}. \end{aligned} \quad (13)$$

Equation (13) is plotted in Fig. 14 as the dash-dotted line. As with the case of forced wetting [1], the simple argument gives a reasonable fit to the data. A rigorous derivation using lubrication theory given by Snoeijer *et al.* [64] gives a nearly identical result as Eq. (13), with a prefactor equal to $\sqrt{3}$. Note that these two arguments both effectively applied the no-shear boundary condition at the liquid-air interface with flux conservation.

For the thin part, for over two orders of magnitude in Ca , Eq. (10) also provides a good fit with

$$\alpha_{\text{thin}} = 0.48 \pm 0.02. \quad (14)$$

Although Eq. (14) is close to that for the thin parts of forced wetting [1], I emphasize that the same stability argument of Ref. [1] does not apply since a key assumption for the argument breaks down in dewetting. In forced wetting, we approximated the velocity of the liquid-air interface near the thin region to be equal to that of the thick region $U_{l,\text{thin}} \approx U_{l,\text{thick}}$. As illustrated in the left panel of Fig. 15, this was reasonable because the thin-thick variation of the air gap is only a small perturbation to the shape of the bulk outer fluid (liquid; shaded area). The outer fluid (liquid) is the dominant fluid except very close to the contact line [61], hence dictating the interface velocity to be roughly uniform regardless of the gap structure. By contrast, in the case of dewetting as illustrated in the right panel of Fig. 15, the inner fluid (liquid; shaded area) plays the dominant role everywhere.

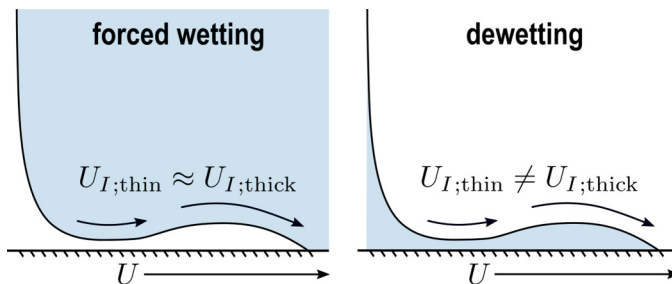


FIG. 15. Left: In forced wetting, the thickness variation of the entrained layer is a perturbation to the dominant bulk liquid, resulting in a roughly equal interface velocity for the thin part $U_{I;\text{thin}}$ and the thick part $U_{I;\text{thick}}$. Right: In dewetting, the thickness variation of the entrained layer is expected to break the uniformity of the interface velocity, making $U_{I;\text{thin}} \neq U_{I;\text{thick}}$ in general.

The prominent thin-thick structure is expected to greatly influence the interface velocity, making the assumption of a simple, uniform interface velocity invalid.

The thin-part thickness also significantly differs from the Landau-Levich-Derjaguin (LLD) theory [5,6,65], which has an exponent:

$$\alpha_{\text{LLD}} = \frac{2}{3}. \quad (15)$$

The LLD prediction is plotted in Fig. 14 as the dashed line for comparison. The measurements deviate from the LLD theory especially at low Ca . In the LLD theory, gravity and viscous dissipation are balanced, and the thickness of an *infinite* liquid layer is uniquely determined by matching the meniscus shape near the bath. Assuming in the current case a similar balance between gravity and viscous dissipation, the discrepancy suggests that the thin-part thickness h_{thin} is not selected by meniscus matching. The existence of the contact line nearby, neighboring thicker parts, and a bounding overall V shape, which are not incorporated in the LLD theory, presumably play important roles. Further modeling is required to quantitatively interpret the result in Eq. (14).

The method of maximum-likelihood fitting is also carried out for the case of wetting. Figure 16(a) shows a laser image of a part of the entrained air film. There are interference fringes which are noisy and have artifacts such as a dust shadow on the bottom left. The air film patch is divided into four smaller parts, each of which can be approximated by a parabolic shape. Our fit for individual parts gives satisfactory results, as shown in the middle image. Notice the slight mismatch near the boundaries of adjacent parts. This indicates the inadequacy of the parabolic model near the edge (rather than the inadequacy of the algorithm). The right-most image shows a simple example of local edge detection for the same pattern, which in general cannot capture the features of main interest, and is not robust against errors. The reconstruction of the topography of the air film is achieved by stitching these data patches together. The result is shown in Fig. 16(b), with perspective views from two different angles.

D. Onset on a wide substrate: Intermediate thickness

Previous theoretical and experimental work (e.g., Refs. [24–26,66,67]) have focused on the thickness of a nonwetting liquid film during the early stages [before completion of the triangular shape of Fig. 3(c)]. They indicated that two different film thicknesses appear during the deposition: a leading ridge whose thickness is determined by the contact angle, followed by a thin LLD film whose thickness is determined by the meniscus. Using the interferometric method discussed above (see Appendix A and Ref. [49]), I have measured the film thickness soon after the onset, long before steady state. The measurement was done on a wide plate with width $w = 37.7$ mm. I plot the result in Fig. 17.

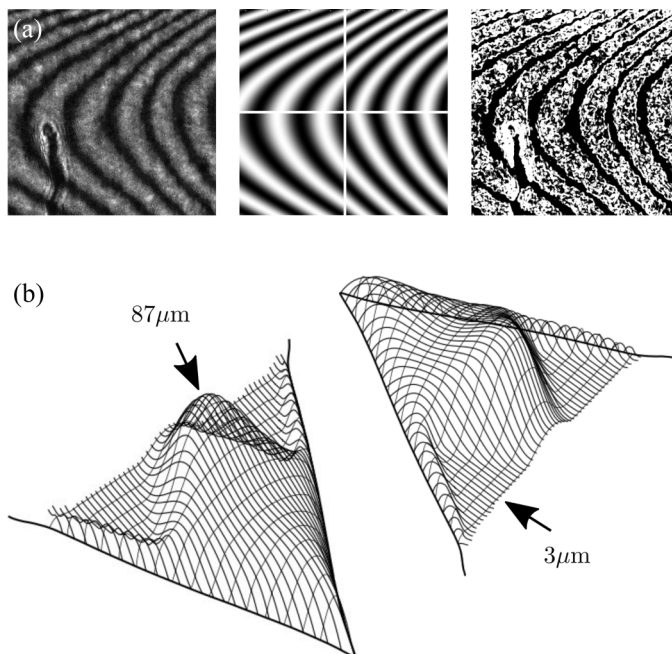


FIG. 16. (a) Fringe fitting using likelihood maximization in forced wetting. Left: Interference fringes of equal height produced by part of an air film (Newton's fringes). Middle: Fringes reconstructed by maximum-likelihood fitting. Frame partitioned into four smaller parts for separate fitting. Right: A typical local edge detection algorithm for comparison. (b) Topography of an air film reconstructed. Peak thickness, $87\ \mu\text{m}$; thin flat part, $3\ \mu\text{m}$. Absolute thickness obtained by using multiwavelength interference discussed in Ref. [1].

During the onset stage, there is a leading thick ridge structure near the contact line, whose thickness is measured and shown as the black diamonds in Fig. 17. The thickness of the ridge structure, h_{ridge} , roughly remains a constant over increasing Ca . This is consistent with the models of Refs. [24,26,67], where h_{ridge} is a function of the *relative* capillary number Ca^* , which does not vary much with the plate velocity (or Ca). I emphasize that the ridge is different from the thick part at steady state, presented in Fig. 14, in both the thickness and the dependence on Ca .

There is an extended thin region of thickness h_{thin} above the meniscus near the bath. It can be fitted to $h_{\text{thin}}/l_c \propto \text{Ca}^{0.59 \pm 0.01}$ (bottom solid line). This thin film is close to the LLD prediction $h_{\text{LLD}}/l_c = 0.946\text{Ca}^{2/3}$ (dashed line), confirming previous studies of the onset of entrainment [64,66,67].

In addition, there appears a region of intermediate thickness h_{int} , which has not been reported in previous works. The thin film of h_{thin} close to the LLD prediction turns out to be only transient. It is left behind immediately after entrainment begins, lasts for a short period, and is rapidly replaced by a region of intermediate thickness h_{int} ($h_{\text{thin}} < h_{\text{int}} < h_{\text{ridge}}$). The thickness change is discontinuous. This process is illustrated in the schematic drawing of Fig. 17(a). The inset of Fig. 17(b) shows an image of the ridge, the intermediate region, and the thin region at the same time soon after entrainment. At low plate velocities, the LLD film may never appear.

The intermediate film can be fitted to $h_{\text{int}}/l_c \propto \text{Ca}^{0.63 \pm 0.02}$ (top solid line). Empirically $h_{\text{int}} \approx 2h_{\text{thin}}$, over two decades of Ca range. When the ridge thickness h_{ridge} approaches the thickness h_{int} of the intermediate region ($\text{Ca} \sim 10^{-2}$ in Fig. 17), the separation of the ridge region and the intermediate film becomes less clear. At high $\text{Ca} > 10^{-2}$, the ridge structure does not appear and the layer behind the contact line assumes a monotonic thickness, which is similar to the result of Ref. [67]. (Note the intermediate region was not considered, so the monotonic film without a

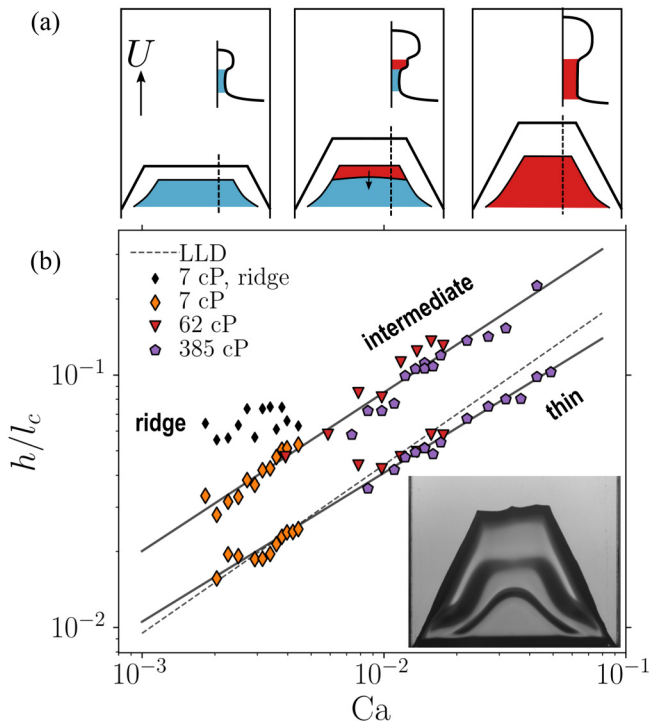


FIG. 17. (a) Schematic showing the formation of a film of intermediate thickness (red) on a wide plate. (b) Measured thickness scaled by capillary length, h/l_c , versus Ca . Top solid line, $h/l_c \propto Ca^{0.63}$; bottom solid line, $h/l_c \propto Ca^{0.59}$. Substrate width $w = 37.7$ mm. Inset: Typical image of onset film, showing the ridge, the intermediate region, and the thin region.

capillary shock occurs at $h_{\text{thin}} = h_{\text{ridge}}$ in their work.) A thicker region behind the contact line will nucleate much later to form the thick parts at steady state such as those of Fig. 3(d) and Fig. 4(b).

When the substrate width w is small, the formation of the intermediate region during the onset is not observed [as is absent from Figs. 3(b) and 3(c) for $w = 20.3$ mm]. A thin film that can be described by the LLD theory is deposited behind a thicker ridge during entrainment before steady state. The above observations of the intermediate region using a wider plate suggest that the plate geometry may impact the morphology of the film structure, which deserves further quantitative investigations.

IV. CONCLUSIONS

I have presented an experimental study on various aspects of dewetting, and have systematically compared the results with those we found in forced-wetting experiments. I have discovered a prominent structure in the layer of steady-state dewetting, consisting of well-defined thin-thick alternations transverse to the direction of substrate motion, behind a V-shaped contact line. This paper draws attention to a possible instability in the spanwise direction in wetting and dewetting, which is not incorporated in most current models.

For both wetting and dewetting, I found quantitatively that the normal relative velocity is larger during the onset than it is at steady state, which extends the previous observations and is different from a fixed maximum contact-line speed in other wetting and dewetting geometries.

To characterize and quantify precisely the thin-thick structure in the dewetting layer, I developed a method, combining interference information from varying the angle of incidence and pattern fitting with maximum-likelihood estimation. Power-law relationships are found between layer thickness h

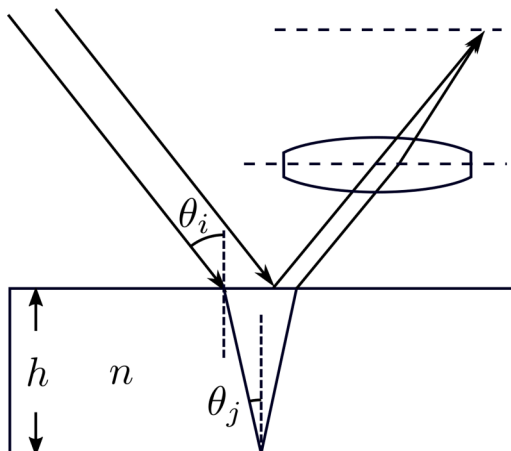


FIG. 18. Schematic of interference produced by a beam with angle of incidence θ_i onto a sample of thickness h . Light reflected from top surface at θ_i and bottom surface at θ_j interferes at the focal plane of a lens placed above.

and capillary number Ca over two decades of Ca range, for different parts of the steady state. The thickness of the steady-state thin part in dewetting differs from various existing models. The new pattern-fitting algorithm also helps to reconstruct the topography of the air layer in forced wetting.

Lastly, onset of dewetting entrainment has been examined and I found a region whose thickness is in between two known regions predicted and observed in various previous studies.

This work shows that dynamic partial wetting is far more complex than accounted for in various simple models. Future work is needed to quantify and understand the contact-line velocity variation as well as the mechanism for thickness selection in both the onset and steady state. Further experiments on wetting in two-liquid systems, where both liquids contribute significantly, can help to examine and clarify the argument of stability.

ACKNOWLEDGMENTS

I am deeply indebted to Sidney R. Nagel for his advising and mentoring. I wish to acknowledge the great help provided by Anthony E. LaTorre on various computational techniques on likelihood maximization from extensive discussions. I am grateful to Chloe W. Lindeman for providing side-view images of sample drops which made Fig. 2(b) possible. The work was primarily supported by the University of Chicago MRSEC, funded by the National Science Foundation under Grant No. DMR-2011854 and by U.S. Department of Commerce, National Institute of Standards and Technology under award 70NANB19H005.

APPENDIX A: MEASUREMENT OF ABSOLUTE THICKNESS: PRINCIPLE

When a parallel beam of light is incident upon a transparent sample of thickness h with an angle of incidence θ_i , the reflected beam from the top surface at angle θ_i and the one from the bottom surface at θ_j are brought together by a lens placed above, as shown in Fig. 18. Interference occurs at the focal plane of the lens. Considering the phase change upon reflection, the optical path difference is $2nh \cos \theta_j + \lambda/2$, where n is the refractive index of the sample and λ is the wavelength of the light source. The intensity of interference depends on the angle of incidence θ_i . When the interference is completely destructive,

$$2nh \cos \theta_j = m\lambda, \quad (\text{A1})$$

where m is an integer indicating the order of the destructive interference. All the rays that produce a single dark fringe correspond to the same value of θ_j . These fringes are fringes of equal inclination. When the angle of incidence is changed from θ_{i1} to θ_{i2} such that the order of interference increases by $\Delta m = 1$, from Eq. (A1) the corresponding θ_{j1} and θ_{j2} satisfy

$$2nh(\cos \theta_{j2} - \cos \theta_{j1}) = \lambda.$$

Since θ_j is related to θ_i through Snell's law,

$$\sin \theta_i = n \sin \theta_j, \quad (\text{A2})$$

we have

$$2nh \left(\cos \arcsin \frac{\sin \theta_{i2}}{n} - \cos \arcsin \frac{\sin \theta_{i1}}{n} \right) = \lambda. \quad (\text{A3})$$

If θ_{i1} and θ_{i2} can be measured, Eq. (A3) gives a determination of h if the index of refraction, n , is known. Notice that no small-angle approximation has been assumed, making the above analysis valid for arbitrary angles of incidence.

In particular, in our setup described in Ref. [49], the interference pattern is a set of concentric rings at the focal plane. θ_j is given by

$$\sin \theta_j = \frac{1}{n} \sqrt{\frac{(x - x_c)^2 + (y - y_c)^2}{(x - x_c)^2 + (y - y_c)^2 + f^2}}, \quad (\text{A4})$$

where f is the focal length of the convex lens, (x, y) is the coordinate at the focal plane, and (x_c, y_c) is the center of the rings.

APPENDIX B: DATA FITTING: LIKELIHOOD MAXIMIZATION

In the thickness measurements, one needs to convert data images of interference fringes to thickness information. It can be extremely difficult to extract fringe patterns from noisy data images. Local edge detection algorithms often perform poorly for patterns whose length scales span multiple orders of magnitude in the presence of a wide range of noise and artifacts (e.g., shadows, lens flares, etc.). An example is shown in the third frame of Fig. 16(a).

Since the physical model, i.e., the relation between fringe configuration and thickness h , is known, I approach this problem using likelihood maximization. For a data image the measured pixel intensity of coordinate (x, y) is $X(x, y)$. The parameters of the model are denoted as β , the log-probability $\log P$ for all pixels of the data image taking the current values is

$$\begin{aligned} \log P &= \log \prod_{x,y} P(X(x, y), \beta) \\ &= \log \prod_{x,y} P(X(x, y)|\beta)P(\beta) \\ &\propto \sum_{x,y} \log P(X(x, y)|\beta). \end{aligned} \quad (\text{B1})$$

In the last step above, $P(\beta)$ is omitted since the model parameter vector β is not a random vector. The best β that fits the data is that which maximizes the log-likelihood $l(\beta) \equiv \sum_{x,y} \log P(X(x, y)|\beta)$ (viewed as a function of β):

$$\beta_{\text{optimal}} = \underset{\beta}{\operatorname{argmax}} l(\beta). \quad (\text{B2})$$

The expression of $l(\beta)$ depends on how the pixel fluctuation is modeled. Consider the simple case of normal distribution $P(X(x, y)|\beta) \propto \exp[-(X(x, y) - X_0(x, y, \beta))^2/\sigma^2]$ where $X_0(x, y, \beta)$ is

the expected pixel intensity from the physical model given a particular vector β . Then we have

$$l(\beta) \propto \sum_{x,y} -(X(x, y) - X_0(x, y, \beta))^2. \quad (\text{B3})$$

Thus, from Eq. (B2)

$$\beta_{\text{optimal}} = \operatorname{argmin}_{\beta} \sum_{x,y} (X(x, y) - X_0(x, y, \beta))^2. \quad (\text{B4})$$

Therefore, under the assumption of normal distribution of pixel intensity, finding the optimal parameter β amounts to a least-squares regression.

In the case of dewetting, we take h , x_c , and y_c as three fitting parameters. Combining Eqs. (A1), (A2), and (A4), the expected intensity $X_0(x, y, \beta)$ is given by

$$\begin{aligned} X_0(x, y, \beta) &= \frac{1}{2} + \frac{1}{2} \cos \left(\frac{2\pi}{\lambda} 2nh \cos \theta_j + \pi \right), \\ \sin \theta_j &= \frac{1}{n} \sqrt{\frac{(x - x_c)^2 + (y - y_c)^2}{(x - x_c)^2 + (y - y_c)^2 + f^2}}, \\ \beta &= (h, x_c, y_c). \end{aligned} \quad (\text{B5})$$

Substituting Eqs. (B5) into Eq. (B4) gives the expression of $\beta_{\text{optimal}} = (h_{\text{optimal}}, x_{c,\text{optimal}}, y_{c,\text{optimal}})$. Since the right-hand side of Eq. (B4) is highly nonconvex, β_{optimal} is found by brute-force searching through all nodes in (h, x_c, y_c) parameter space, with step resolution $\delta h = \lambda/(4n)$, $\delta x_c = \delta y_c = 1$ pixel. With known centers $(x_{c,a}, y_{c,a})$ and $(x_{c,b}, y_{c,b})$, an exhaustive search in the parameter space $\beta = (h, h + p\lambda/2n, n)$ to maximize the joint likelihood of the two frames [summation over all pixels for two frames in Eq. (B4)] gives the optimal n .

Similarly for the case of forced wetting, I use normal incidence only and model the interference fringes of equal height. The patterned area is divided into smaller parts, whose thickness can be approximated by a quadratic expansion. This is shown in Eqs. (B6). Since there are six components to optimize in β of this model, I use a basin-hopping minimizing algorithm instead of brute-force searching:

$$\begin{aligned} X_0(x, y, \beta) &= \frac{1}{2} + \frac{1}{2} \cos \left(\frac{2\pi}{\lambda} 2nh(x, y, \beta) + \pi \right), \\ h(x, y, \beta) &= \beta_1 x^2 + \beta_2 y^2 + \beta_3 xy + \beta_4 x + \beta_5 y + \beta_6, \\ \beta &= (\beta_1, \beta_2, \beta_3, \beta_4, \beta_5, \beta_6). \end{aligned} \quad (\text{B6})$$

-
- [1] M. He and S. R. Nagel, Characteristic Interfacial Structure Behind a Rapidly Moving Contact Line, *Phys. Rev. Lett.* **122**, 018001 (2019).
- [2] D. Bonn, J. Eggers, J. Indekeu, J. Meunier, and E. Rolley, Wetting and spreading, *Rev. Mod. Phys.* **81**, 739 (2009).
- [3] R. Ablett, XXV. An investigation of the angle of contact between paraffin wax and water, *London, Edinburgh Dublin Philos. Mag. J. Sci.* **46**, 244 (1923).
- [4] R. N. Wenzel, Resistance of solid surfaces to wetting by water, *Ind. Eng. Chem.* **28**, 988 (1936).
- [5] L. D. Landau and B. V. Levich, Dragging of a liquid by a moving plate, *Acta Physicochim. URSS* **17**, 42 (1942).
- [6] B. Derjaguin, Thickness of liquid layer adhering to walls of vessels on their emptying and the theory of photo-and motion-picture film coating, *C. R. (Dokl.) Acad. Sci. URSS* **39**, 13 (1943).

- [7] D. White and J. Tallmadge, Theory of drag out of liquids on flat plates, *Chem. Eng. Sci.* **20**, 33 (1965).
- [8] S. D. Wilson, The drag-out problem in film coating theory, *J. Eng. Math.* **16**, 209 (1982).
- [9] B. V. Derjaguin and S. M. Levi, *Film Coating Theory* (Focal Press, London, 1964).
- [10] W. Wilkinson, Entrainment of air by a solid surface entering a liquid/air interface, *Chem. Eng. Sci.* **30**, 1227 (1975).
- [11] R. Burley and B. Kennedy, An experimental study of air entrainment at a solid/liquid/gas interface, *Chem. Eng. Sci.* **31**, 901 (1976).
- [12] T. Blake and K. Ruschak, A maximum speed of wetting, *Nature (London)* **282**, 489 (1979).
- [13] R. Burley and R. Jolly, Entrainment of air into liquids by a high speed continuous solid surface, *Chem. Eng. Sci.* **39**, 1357 (1984).
- [14] H. Benkreira and M. Khan, Air entrainment in dip coating under reduced air pressures, *Chem. Eng. Sci.* **63**, 448 (2008).
- [15] H. Benkreira and J. Ikin, Dynamic wetting and gas viscosity effects, *Chem. Eng. Sci.* **65**, 1790 (2010).
- [16] E. Guttoff and C. Kendrick, Dynamic contact angles, *AIChE J.* **28**, 459 (1982).
- [17] R. Sedev and J. Petrov, The critical condition for transition from steady wetting to film entrainment, *Colloids Surf.* **53**, 147 (1991).
- [18] J. G. Petrov and P. G. Petrov, Forced advancement and retraction of polar liquids on a low energy surface, *Colloids Surf.* **64**, 143 (1992).
- [19] J. A. Marsh, S. Garoff, and E. B. Dussan V., Dynamic Contact Angles and Hydrodynamics near a Moving Contact Line, *Phys. Rev. Lett.* **70**, 2778 (1993).
- [20] E. Vandre, M. S. Carvalho, and S. Kumar, Delaying the onset of dynamic wetting failure through meniscus confinement, *J. Fluid Mech.* **707**, 496 (2012).
- [21] E. Vandre, M. Carvalho, and S. Kumar, Characteristics of air entrainment during dynamic wetting failure along a planar substrate, *J. Fluid Mech.* **747**, 119 (2014).
- [22] O. Kim and J. Nam, Confinement effects in dip coating, *J. Fluid Mech.* **827**, 1 (2017).
- [23] J. Eggers, Hydrodynamic Theory of Forced Dewetting, *Phys. Rev. Lett.* **93**, 094502 (2004).
- [24] J. H. Snoeijer, B. Andreotti, G. Delon, and M. Fermigier, Relaxation of a dewetting contact line. Part 1. A full-scale hydrodynamic calculation, *J. Fluid Mech.* **579**, 63 (2007).
- [25] G. Delon, M. Fermigier, J. H. Snoeijer, and B. Andreotti, Relaxation of a dewetting contact line. Part 2. Experiments, *J. Fluid Mech.* **604**, 55 (2008).
- [26] J. H. Snoeijer, G. Delon, M. Fermigier, and B. Andreotti, Avoided Critical Behavior in Dynamically Forced Wetting, *Phys. Rev. Lett.* **96**, 174504 (2006).
- [27] T. S. Chan, J. H. Snoeijer, and J. Eggers, Theory of the forced wetting transition, *Phys. Fluids* **24**, 072104 (2012).
- [28] J. Qin and P. Gao, Asymptotic theory of fluid entrainment in dip coating, *J. Fluid Mech.* **844**, 1026 (2018).
- [29] C. Kamal, J. E. Sprittles, J. H. Snoeijer, and J. Eggers, Dynamic drying transition via free-surface cusps, *J. Fluid Mech.* **858**, 760 (2019).
- [30] F. P. Bretherton, The motion of long bubbles in tubes, *J. Fluid Mech.* **10**, 166 (1961).
- [31] G. I. Taylor, Deposition of a viscous fluid on the wall of a tube, *J. Fluid Mech.* **10**, 161 (1961).
- [32] A. De Ryck and D. Quéré, Inertial coating of a fibre, *J. Fluid Mech.* **311**, 219 (1996).
- [33] B. Zhao, A. Alizadeh Pahlavan, L. Cueto-Felgueroso, and R. Juanes, Forced Wetting Transition and Bubble Pinch-Off in a Capillary Tube, *Phys. Rev. Lett.* **120**, 084501 (2018).
- [34] P. Gao, A. Liu, J. J. Feng, H. Ding, and X.-Y. Lu, Forced dewetting in a capillary tube, *J. Fluid Mech.* **859**, 308 (2019).
- [35] T. Podgorski, J.-M. Flesselles, and L. Limat, Corners, Cusps, and Pearls in Running Drops, *Phys. Rev. Lett.* **87**, 036102 (2001).
- [36] L. Limat and H. A. Stone, Three-dimensional lubrication model of a contact line corner singularity, *Europhys. Lett.* **65**, 365 (2004).
- [37] N. Le Grand, A. Daerr, and L. Limat, Shape and motion of drops sliding down an inclined plane, *J. Fluid Mech.* **541**, 293 (2005).

- [38] E. Rio, A. Daerr, B. Andreotti, and L. Limat, Boundary Conditions in the Vicinity of a Dynamic Contact Line: Experimental Investigation of Viscous Drops Sliding Down an Inclined Plane, *Phys. Rev. Lett.* **94**, 024503 (2005).
- [39] J. H. Snoeijer, E. Rio, N. Le Grand, and L. Limat, Self-similar flow and contact line geometry at the rear of cornered drops, *Phys. Fluids* **17**, 072101 (2005).
- [40] J. Snoeijer, N. Le Grand-Piteira, L. Limat, H. A. Stone, and J. Eggers, Cornered drops and rivulets, *Phys. Fluids* **19**, 042104 (2007).
- [41] I. Peters, J. H. Snoeijer, A. Daerr, and L. Limat, Coexistence of Two Singularities in Dewetting Flows: Regularizing the Corner Tip, *Phys. Rev. Lett.* **103**, 114501 (2009).
- [42] K. Winkels, I. Peters, F. Evangelista, M. Riepen, A. Daerr, L. Limat, and J. H. Snoeijer, Receding contact lines: From sliding drops to immersion lithography, *Eur. Phys. J.: Spec. Top.* **192**, 195 (2011).
- [43] L. Limat, Drops sliding down an incline at large contact line velocity: What happens on the road towards rolling? *J. Fluid Mech.* **738**, 1 (2014).
- [44] Soap and Detergent Association, Glycerine: An Overview: Terms, Technical Data, Properties, Performance, Soap and Detergent Association report, 1990 (unpublished), http://www.aciscience.org/docs/glycerine_-_an_overview.pdf.
- [45] K. Takamura, H. Fischer, and N. R. Morrow, Physical properties of aqueous glycerol solutions, *J. Pet. Sci. Eng.* **98–99**, 50 (2012).
- [46] N.-S. Cheng, Formula for the viscosity of a glycerol-water mixture, *Ind. Eng. Chem. Res.* **47**, 3285 (2008).
- [47] Side-view images provided by Chloe W. Lindeman.
- [48] L. Hoyt, New table of the refractive index of pure glycerol at 20 °C, *Ind. Eng. Chem.* **26**, 329 (1934).
- [49] M. He and S. R. Nagel, Determining the refractive index, absolute thickness and local slope of a thin transparent film using multi-wavelength and multi-incident-angle interference, *Opt. Express* **28**, 24198 (2020).
- [50] J. W. Strutt, 3rd Baron Rayleigh, LIV. On the interference-rings, described by Haidinger, observable by means of plates whose surfaces are absolutely parallel, *London, Edinburgh Dublin Philos. Mag. J. Sci.* **12**, 489 (1906).
- [51] C. Raman and V. Rajagopalan, L. Haidinger's rings in non-uniform plates, *London, Edinburgh Dublin Philos. Mag. J. Sci.* **29**, 508 (1940).
- [52] N. Gold, D. L. Willenborg, J. Opsal, and A. Rosencwaig, Method and apparatus for measuring thickness of thin films U.S. Patent No. 4,999,014 (12 March 1991).
- [53] J.-a. Kim, J.-W. Kim, J.-Y. Lee, and J.-H. Woo, Thickness measuring apparatus and thickness measuring method U.S. Patent No. 9,927,224 (27 March 2018).
- [54] p -value > 0.05 ; also notice γ and θ_r are linearly related through Eqs. (1) and (2) so there is no need to further test $U_{n,\text{fit}} \propto \eta^\alpha \gamma^\beta \theta_r^\gamma$.
- [55] O. Voinov, Hydrodynamics of wetting, *Fluid Dyn.* **11**, 714 (1976).
- [56] R. G. Cox, The dynamics of the spreading of liquids on a solid surface. Part 1. Viscous flow, *J. Fluid Mech.* **168**, 169 (1986).
- [57] P.-G. de Gennes, Deposition of Langmuir-Blodgett layers, *Colloid Polym. Sci.* **264**, 463 (1986).
- [58] E. Dussan, On the spreading of liquids on solid surfaces: Static and dynamic contact lines, *Annu. Rev. Fluid Mech.* **11**, 371 (1979).
- [59] F. Brochard-Wyart and P. de Gennes, Dynamics of partial wetting, *Adv. Colloid Interface Sci.* **39**, 1 (1992).
- [60] C. Huh and L. Scriven, Hydrodynamic model of steady movement of a solid/liquid/fluid contact line, *J. Colloid Interface Sci.* **35**, 85 (1971).
- [61] A. Marchand, T. S. Chan, J. H. Snoeijer, and B. Andreotti, Air Entrainment by Contact Lines of a Solid Plate Plunged into a Viscous Fluid, *Phys. Rev. Lett.* **108**, 204501 (2012).
- [62] The coefficient C_1 given by the linear fit in Fig. 10 seems to give an overly small $q \in [-0.5, 0.1]$, where q is the exponent of the modeled interface profile $h(x)$ at the contact line $h \sim x^{1/2} + x^q$.
- [63] J. Eggers, Existence of receding and advancing contact lines, *Phys. Fluids* **17**, 082106 (2005).

- [64] J. H. Snoeijer, J. Ziegler, B. Andreotti, M. Fermigier, and J. Eggers, Thick Films of Viscous Fluid Coating a Plate Withdrawn from a Liquid Reservoir, [Phys. Rev. Lett. **100**, 244502 \(2008\)](#).
- [65] V. G. Levich, *Physicochemical Hydrodynamics* (Prentice-Hall, Englewood Cliffs, NJ, 1962), Vol. 115.
- [66] M. Maleki, M. Reyssat, F. Restagno, D. Quéré, and C. Clanet, Landau-Levich menisci, [J. Colloid Interface Sci. **354**, 359 \(2011\)](#).
- [67] P. Gao, L. Li, J. J. Feng, H. Ding, and X.-Y. Lu, Film deposition and transition on a partially wetting plate in dip coating, [J. Fluid Mech. **791**, 358 \(2016\)](#).